# Critical behavior of van der Waals topological ferromagnet CrVI$_6$ ⊘

Qiaoqiao Wang (ID) ; Hanzhang Zhao; Xuegang Chen (ID) ; Feiyan Hou (ID) ; Tao Li ✉ (ID) ; Tai Min ✉

Check for updates

View Online    Export Citation

## Articles You May Be Interested In

**Applied Physics Letters**

AIP Publishing

# Critical behavior of van der Waals topological ferromagnet CrVI$_6$

View Online   Export Citation   CrossMark

Qiaoqiao Wang,[1] (iD) Hanzhang Zhao,[1] Xuegang Chen,[2] (iD) Feiyan Hou,[1] (iD) Tao Li,[1,a] (iD) and Tai Min[1,3,a]

### AFFILIATIONS

[1]Center for Spintronics and Quantum Systems, State Key Laboratory for Mechanical Behavior of Materials,
School of Materials Science and Engineering, Xi'an Jiaotong University, Xi'an, Shaanxi 710049, China

[2]Information Materials and Intelligent Sensing Laboratory of Anhui Province, Center of Free Electron Laser & High Magnetic Field,
Anhui University, Hefei 230601, China

[3]National Laboratory of Solid-State Microstructures, School of Materials Science and Intelligent Engineering,
Nanjing University, Suzhou 215163, China

[a]Authors to whom correspondence should be addressed: taoli66@xjtu.edu.cn and tai.min@nju.edu.cn

### ABSTRACT

CrVI$_6$ is a recently proposed van der Waals topological magnetic material derived from its parent compounds, CrI$_3$ and VI$_3$, via elemental substitution. However, beyond initial proposals of its topological nature, the fundamental characteristics of its magnetic ordering remain largely unexplored. Investigating the critical behaviors of a magnet provides deep insight into its underlying spin interactions and universality class. In this work, we synthesized high-quality CrVI$_6$ single crystals, demonstrating strong perpendicular magnetic anisotropy below the Curie temperature ($\sim$58.2 K) via DC magnetization and heat capacity measurements. The critical magnetic behavior in the vicinity of the paramagnetic to ferromagnetic phase transition region has been systematically analyzed using multiple approaches, yielding the critical exponents $\beta = 0.294(8)$, $\gamma = 0.947(9)$, and $\delta = 4.21(5)$. These values do not conform to any single universality class but instead demonstrate a distinct crossover behavior between the three-dimensional Ising and tricritical mean-field models. This crossover is indicative of complex magnetic ordering, characterized by the coexistence of short-range and long-range exchange interactions. Further analysis using renormalization group theory quantifies the decay of the exchange interaction $J(r) \approx r^{-4.80}$, confirming the behavior consistent with the crossover model. Our findings establish a comprehensive picture of the fundamental spin correlations in CrVI$_6$, highlighting it as a fertile platform for developing future quantum and spintronic applications.

Since the discovery of two-dimensional (2D) ferromagnetic CrI$_3$[1] and Cr$_2$Ge$_2$Te$_6$[2] in 2017, significant research efforts have been devoted to exploring various 2D magnetic materials, such as Fe$_3$GeTe$_2$,[3] CrBr$_3$,[4] VI$_3$,[5,6] and MnBi$_2$Te$_4$[7] with relatively low Curie temperature (T$_C$), as well as CrTe$_2$,[8] Fe$_3$GaTe$_2$,[9] and FeCr$_{0.5}$Ga$_{1.5}$Se$_4$[10] with T$_C$ above room temperature. These recently discovered 2D magnets promote the development of spintronic devices.[11–18] CrI$_3$ is one of the most studied 2D magnets. It is a 2D trihalide exhibiting T$_C$ of 61 K in the bulk form and 45 K in the monolayer.[1] CrI$_3$ has a rhombohedral BiI$_3$ structure, and each Cr ion is centered in an octahedron of I ions, forming a honeycomb lattice in the ab-plane.[19] Few-layer CrI$_3$ has layer number-dependent magnetic properties due to the intralayer ferromagnetic coupling and interlayer antiferromagnetic coupling.[1,20,21] Another member of 2D trihalides is VI$_3$, which is an insulating ferromagnet with a T$_C$ of 50 K in bulk, while a higher T$_C$ (57 K) was

observed in a few-layer VI$_3$ tunneling device.[22] VI$_3$ has a crystal structure similar to CrI$_3$, but no layer-dependent magnetism has been revealed.[5,6] VI$_3$ and CrI$_3$ have good structural compatibility but distinct magnetization, leading to the potential design of 2D magnetic materials by element mutation of V and Cr atoms.

CrVI$_6$ has been theoretically proposed to be a topological nontrivial Chern insulator exhibiting the high-temperature quantum anomalous Hall effect in 2021.[23] In the next year, Pan *et al.* synthesized CrVI$_6$ crystals (T$_C$ $\sim$55 K), the magnetic crystal anisotropy and coercivity of which are increased compared to the parent CrI$_3$, showing the characteristics of hard magnets.[24] Recently, Li *et al.* observed the topological Kerr effect in CrVI$_6$ films due to the broken in-plane inversion symmetry,[25] which experimentally proved the topologically nontrivial nature of CrVI$_6$. Although some initial theoretical and experimental research has been conducted on the topological effects in CrVI$_6$, systematic

investigations of the magnetic phase transition and spin interactions in $CrVI_6$ are still scarce. Analysis of critical behaviors is an important approach to gaining deep insight into the fundamental nature of magnetic interactions and the universality class of $CrVI_6$, which is also helpful in understanding the origin of the topological effects.[26–29]

Here, we performed detailed investigations of the fundamental magnetic properties and the critical behaviors of the $CrVI_6$ crystal. The synthesized crystal has demonstrated strong perpendicular magnetic anisotropy (PMA) below its $T_C$ (~58.2 K). The critical behaviors of $CrVI_6$ were analyzed using critical isotherm (CI), Kouvel–Fisher plot (KFP), modified Arrott plot (MAP), iterative modified Arrott plot (iMAP), and magnetic entropy change (MEC) methods. The optimized critical exponents are obtained as $\beta = 0.294(8)$, $\gamma = 0.947(9)$, and $\delta = 4.21(5)$, which fall into the range exhibiting crossover between the 3D Ising model and the tricritical mean-field model, demonstrating complex magnetic interactions with the coexistence of short-range and long-range interactions in $CrVI_6$ with interlayer coupling. This is also confirmed by the magnetic exchange interaction, which decays with the distance between spins as $J(r) \approx r^{-4.80}$. Such strong uniaxial anisotropy combined with complex magnetic interactions could be the potential driving force of the topological spin texture.

The $CrVI_6$ crystals were synthesized by chemical vapor transport (CVT) (experimental details see the supplementary material). The x-ray diffraction (XRD) spectrum of the crystal demonstrates typical layered features [Fig. 1(a)], with diffraction peaks indexed to the (00l) family, consistent with those reported in the literature.[24,25] Elemental analysis by energy dispersive x-ray (EDX) demonstrates that Cr, V, and I elements are uniformly distributed [Fig. 1(b)] without phase separation between $CrI_3$ and $VI_3$ at this resolution scale. Figure 1(c) shows the EDX spectrum of the $CrVI_6$ crystal, based on which the atomic ratio of the crystal is determined to be $Cr:V:I = 0.91:1.09:6$, close to the designed ratio of 1:1:6.

DC magnetization measurements were performed to explore the magnetic phase transition of the $CrVI_6$ crystal. Figure 2(a) shows the temperature-dependent zero-field-cooled (ZFC) and field-cooled (FC) magnetization curve $M(T)$ with a 1000 Oe magnetic field applied along the ab-plane and c axis. An abrupt increase in the magnetic

moment indicates the paramagnetic (PM) to the ferromagnetic (FM) phase transition near $T_C$, which is determined to be 58 K based on the $dM/dT$ plot [inset of Fig. 2(a)]. The observed $T_C$ of the $CrVI_6$ crystal lies between those of $CrI_3$ ($T_C = 61$ K)[1] and $VI_3$ ($T_C = 50$ K) crystals.[6] Below $T_C$, the out-of-plane (OOP) magnetic moment is an order of magnitude larger than the in-plane (IP) moment, demonstrating strong PMA with the c axis as the easy axis. Subsequently, we also measured magnetic hysteresis loops at different temperatures. When the external magnetic field was applied along the c axis (H//c), decent square-shaped magnetic hysteresis loops were observed at temperatures below $T_C$ [Fig. 2(b)]. In contrast, highly inclined unsaturated loops were obtained when H//ab [Fig. 2(c)], again demonstrating the PMA of the $CrVI_6$ crystal.

Subsequently, heat capacity was measured to characterize the phase transition of the $CrVI_6$ crystals. Figure 2(d) shows the zero-field heat capacity curve of $CrVI_6$ in the cooling-temperature mode [$C_P(T)$], where a pronounced peak appears at 58 K, consistent with the $T_C$ obtained from the $M(T)$ curve. Furthermore, the heat capacity curves near $T_C$ under different external magnetic fields [Fig. 2(e)] were measured. It reveals that as the magnetic field increases, the lambda-like feature at $T_C$ shifts to higher temperatures and broadens, which typically signifies a second-order ferromagnetic phase transition.[30] Similar behavior has been observed in $CrI_3$ and $VI_3$.[6,19,31–34] Additionally, the heat capacity change $\Delta C_P$ defined as $C_P(T, H) - C_P(T, 0)$[35] under different magnetic fields is shown in Fig. 2(f). As the temperature decreases, $\Delta C_P$ transforms from positive values in the PM phase to negative values in the FM phase. The temperature at the intersection point with the horizontal axis can be accurately determined as $T_C$, which is 58.2 K.

The study of critical behavior is essential for uncovering the universality laws of phase transitions in complex systems. Critical exponents serve as quantitative tools to characterize these laws, functioning to characterize and correlate critical behaviors of different physical quantities, define universality classes, and validate theoretical models.[36–38]

For magnetic phase transitions, these critical exponents depend solely on order parameter symmetry and lattice dimensionality,
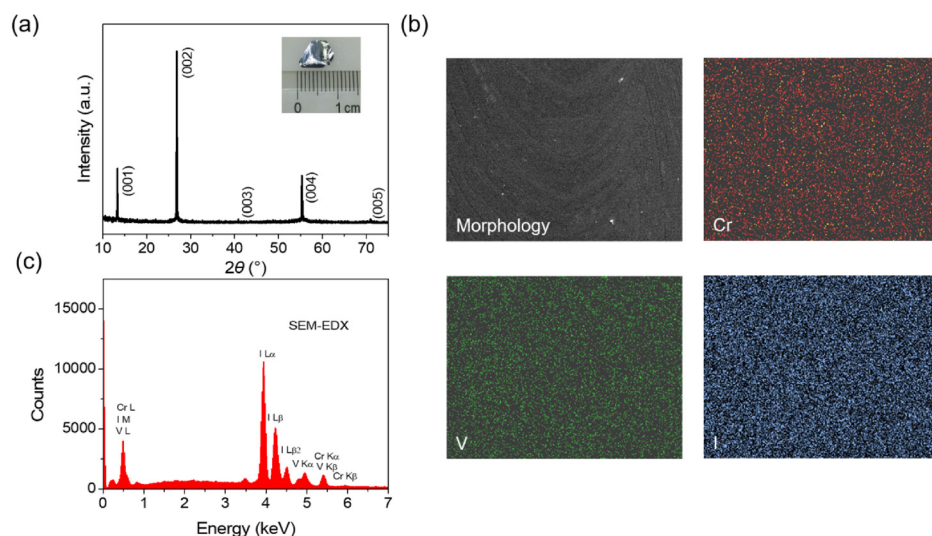


**FIG. 1.** (a) XRD patterns of $CrVI_6$ single crystal demonstrating 2D layered characteristics. The inset is an optical image of a typical $CrVI_6$ crystal. (b) Scanning electron microscopy image of morphology and the elemental distributions of $CrVI_6$. (c) EDX spectrum of the $CrVI_6$ crystal.
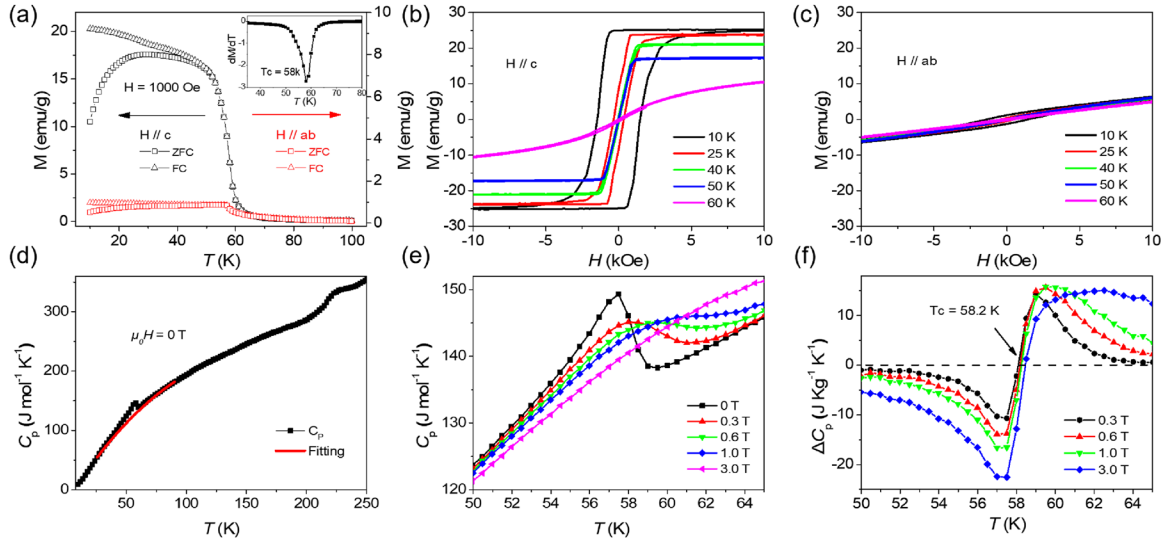
**FIG. 2.** (a) Temperature dependence of field-cooled and zero-field-cooled magnetization $M(T)$ curves for a $CrVI_6$ crystal when H//c and H//ab. The inset shows the derivative of $M(T)$ curve with respect to temperature under field-cooled mode when H//c. (b) Magnetic hysteresis loops of a $CrVI_6$ crystal taken at different temperatures when the magnetic field was applied along the c axis, as well as in the ab-plane (c). (d) Heat capacity $C_P(T)$ curve for a $CrVI_6$ crystal at zero external magnetic field. The red curve represents the lattice contribution fitted by a second-order polynomial. (e) $C_P$ and (f) the $\Delta C_P$ as a function of temperatures in the vicinity of $T_C$ while applying different external magnetic fields.

independent of the microscopic details of the homogeneous magnet. Physically, they provide crucial insights into spin dimensionality, magnetic interactions, correlation length, and spatial decay of the correlation function.[39,40] For magnetic materials, their critical behavior is typically characterized by the critical exponents $\beta$, $\gamma$, and $\delta$, which are related to the spontaneous magnetization $M_S$ below $T_C$, the inverse initial susceptibility $\chi_0^{-1}$ above $T_C$, and the initial isothermal magnetization at $T_C$, respectively. These critical exponents are defined by the following relations:[38]

$$M_S(T) = M_0(-\varepsilon)^{\beta}, \quad \varepsilon < 0, \quad T < T_C, \tag{1}$$

$$\chi_0^{-1}(T) = (h_0/m_0)\varepsilon^{\gamma}, \quad \varepsilon > 0, \quad T > T_C, \tag{2}$$

$$M = DH^{(1/\delta)}, \quad \varepsilon = 0, \quad T = T_C, \tag{3}$$

where $\varepsilon = (T - T_C)/T_C$ is the reduced temperature, and $M_0$, $h_0/m_0$, and $D$ are the critical amplitudes.[41] After several decades of development, these critical exponents can now be determined through multiple approaches, including CI,[38] KFP,[42] MAP,[43] iMAP,[44] and MEC.[45] Notably, the initial isothermal magnetization curves around $T_C$ provide essential experimental data for analyzing critical behavior using these methods, with the $CrVI_6$ results specifically presented in Fig. 3(a).

Based on Eqs. (1)–(3), the CI and KFP methods are early approaches for determining critical exponents. The CI method, developed based on Eq. (3), determines the critical exponent $\delta$ by the power-law fitting of the initial isothermal magnetization curve at $T_C$. The fitting results of $CrVI_6$ are presented in Fig. 3(b), yielding $\delta = 3.923(8)$. Although this method demonstrates excellent fitting, it can only determine a single critical exponent and fails to fully characterize the critical behavior of the system. The KFP method was developed by analytically differentiating and reformulating Eqs. (1) and (2) into the following expression:[42]

$$\frac{M_S(T)}{dM_S(T)/dT} = \frac{T - T_C}{\beta}, \tag{4}$$

$$\frac{\chi_0^{-1}(T)}{d\chi_0^{-1}(T)/dT} = \frac{T - T_C}{\gamma}. \tag{5}$$

Based on this method, $\frac{M_S(T)}{dM_S(T)/dT}$ and $\frac{\chi_0^{-1}(T)}{d\chi_0^{-1}(T)/dT}$ are linear functions of temperature with slopes of $1/\beta$ and $1/\gamma$, respectively, while the critical exponent $\delta$ can be obtained through Widom's scaling relation,[46]

$$\delta = 1 + \frac{\gamma}{\beta}. \tag{6}$$

The specific process for obtaining the critical exponent of $CrVI_6$ through the KFP method is as follows: First, the $M_S$ and $\chi_0^{-1}$ are acquired by replotting the isothermal magnetization curves around $T_C$ [Fig. 3(a)] as the Arrott plot[47] [$M^2$ vs H/M, Fig. S2(a) in the supplementary material] based on mean-field theory. Linear fitting of the high-field regions of the Arrott plot (Fig. S1 in the supplementary material) yields the $M_S$ from the y-intercept of isotherms for $T < T_C$ (black line of Fig. S1 in the supplementary material) and the $\chi_0^{-1}$ from the x-intercept of isotherms for $T > T_C$ (red lines of Fig. S1 in the supplementary material). Then, the $M_S$ and $\chi_0^{-1}$ were fitted using Eqs. (4) and (5) to determine the critical exponents $\beta$ and $\gamma$. The fitted results are shown in Fig. 3(c), where the critical exponent $\beta = 0.295(7)$ with $T_C = 59.74(9)$ K, $\gamma = 0.904(6)$ with $T_C = 59.77(3)$ K, and combined with Eq. (6), $\delta = 4.05(9)$. Here, the acquisition of $\delta$ reflects the scaling law-determined correlations among critical exponents and is inherently dependent on the fitting accuracy of $\gamma$ and $\beta$, which may underlie the observed differences in $\delta$ values obtained via the KFP and CI methods. Then, combining the power-law behavior of magnetic parameters described by Eqs. (1)–(3) with the correlations among
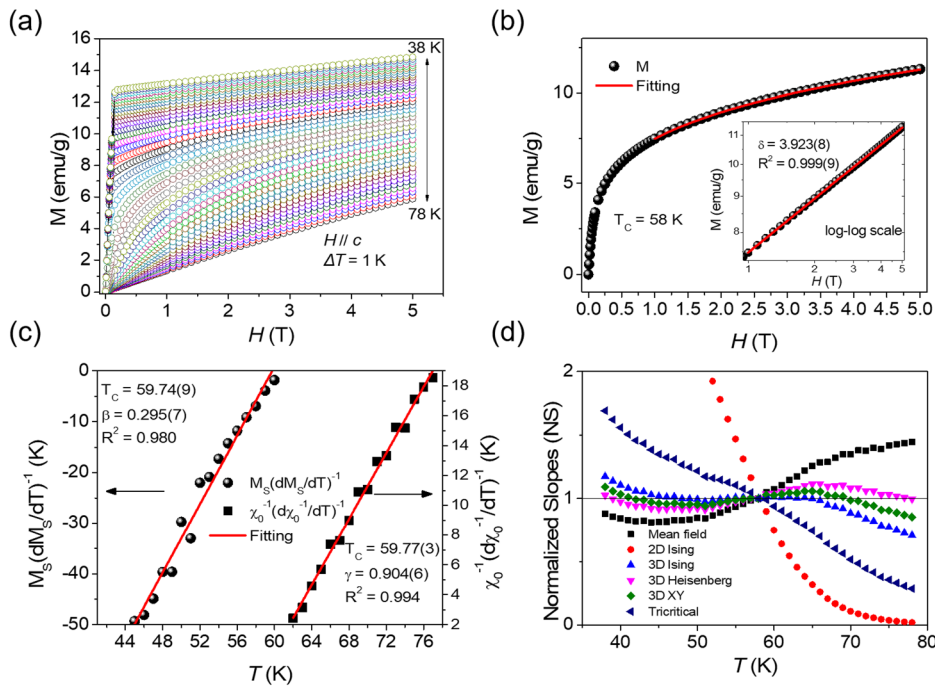
**FIG. 3.** (a) Initial isothermal magnetization curves of $CrVI_6$ when the magnetic field was applied along the c axis from 38 to 78 K with a temperature step of 1 K. (b) Initial isothermal magnetization curve at $T_C$. Inset is the same plot in the log–log scale. (c) The KFP model fitting of $\frac{M_S(T)}{dM_S(T)/dT}$ (left) and $\frac{\chi_0^{-1}(T)}{d\chi_0^{-1}(T)/dT}$ (right). (d) Temperature dependence of the normalized slopes for different models.

critical exponents described by Eq. (6), the magnetic behaviors in the vicinity of $T_C$ can be characterized by the Arrott–Noakes equation,[43]

$$(H/M)^{1/\gamma} = a\varepsilon + bM^{1/\beta}, \qquad (7)$$

where a and b are constants. Based on Eq. (7), the MAP method was established as an analytical framework for determining critical behavior through phenomenological comparison with established universal classes. The specific procedure of the MAP method involves substituting the critical exponents of the given universal models into Eq. (7) to reconstruct isothermal magnetization curves around $T_C$ [Fig. 3(a)] to modify Arrott plots with $(H/M)^{1/\gamma}$ as the x axis and $M^{1/\beta}$ as the y axis (where $\beta = 0.5$ and $\gamma = 1$ correspond to the Arrott plot of the mean-field model). When the critical behavior of the system matches a universal model, the corresponding modified Arrott plot will exhibit a series of linear parallel lines close to $T_C$ in the high-field region, with the line at $T_C$ passing through the origin point. For the MAP method, the Arrott plot of the mean-field model ($\beta = 0.5$ and $\gamma = 1.0$) and the modified Arrott plots for universal classes, 2D Ising model ($\beta = 0.125$, $\gamma = 1.75$), 3D Ising model ($\beta = 0.325$, $\gamma = 1.24$), 3D Heisenberg model ($\beta = 0.365$, $\gamma = 1.386$), 3D XY model ($\beta = 0.345$, $\gamma = 1.316$), and tricritical mean-field model ($\beta = 0.25$, $\gamma = 1.0$),[37,48] were used to analyze the critical behaviors of $CrVI_6$ [Figs. S2(a)–S2(f) in the supplementary material]. To find the best fit, the slope corresponding to the curve is normalized in the high-field region to evaluate the parallelism of the curve. The slope is defined as $S(T) = dM^{1/\beta}/d(H/M)^{1/\gamma}$, and the normalized slopes $NS = S(T)/S(T_C)$ of different models are shown in Fig. 3(d). Apparently, the critical behavior of $CrVI_6$ does not belong to any single universality class. However, the 3D XY, 3D Ising, and 3D Heisenberg models show results much closer to 1, demonstrating the non-negligible interlayer coupling and short-range interactions in the $CrVI_6$ crystal.

To obtain self-consistent results that match experimental data, the iMAP method is widely employed. This approach begins by constructing an initial MAP using a set of starting critical exponents ($\gamma = 1$, $\beta = 0.5$ used for $CrVI_6$). The $M_S$ and $\chi_0^{-1}$ are then determined through high-field linear extrapolation of the MAP, following the same procedure as that in the KFP method. These derived quantities are subsequently fitted using Eqs. (1) and (2) to generate refined estimates of $\gamma$ and $\beta$. Then, the obtained $\beta$ and $\gamma$ are used to construct the MAP again for the next fitting. The entire process is iteratively repeated until the critical exponents converge to stable values. The critical exponents obtained by this method are independent of the initial values, avoiding unphysical fitting and systematic errors.[44,49–53] This method also preserves the scaling relations between critical exponents throughout the iterative process. Using the iMAP method, the final optimal critical exponents of the $CrVI_6$ crystal are obtained [Fig. 4(a) shows the stable fitting results obtained from the last iteration]. The estimated stationary values of critical exponents are $\beta = 0.294(8)$ with $T_C = 57.80(6)$ K, $\gamma = 0.947(9)$ with $T_C = 57.55(9)$ K, and according to Eq. (6), $\delta = 4.21(5)$. Simultaneously, the obtained critical exponents were substituted into the modified Arrott plot to yield optimized results [Fig. 4(b)], which reveal a series of parallel lines with data of $T_C$ intersecting the origin, validating the values of $\beta$ and $\gamma$. The reliability of the critical exponents obtained by the iMAP method can be further proved by the scaling equation, which is also an important criterion for judging the critical state and the correctness of the critical exponents. It can be expressed as[37]

$$M(H, \varepsilon) = \varepsilon^\beta f_\pm(H/\varepsilon^{\beta+\gamma}), \qquad (8)$$

where $f_\pm$ are regular functions ($f_+$ for $T > T_C$ and $f_-$ for $T < T_C$). Equation (8) can be rewritten as $m = f_\pm(h)$ with the renormalized magnetization $m = \varepsilon^\beta M(H, \varepsilon)$ and renormalized field $h = H/\varepsilon^{\beta+\gamma}$.
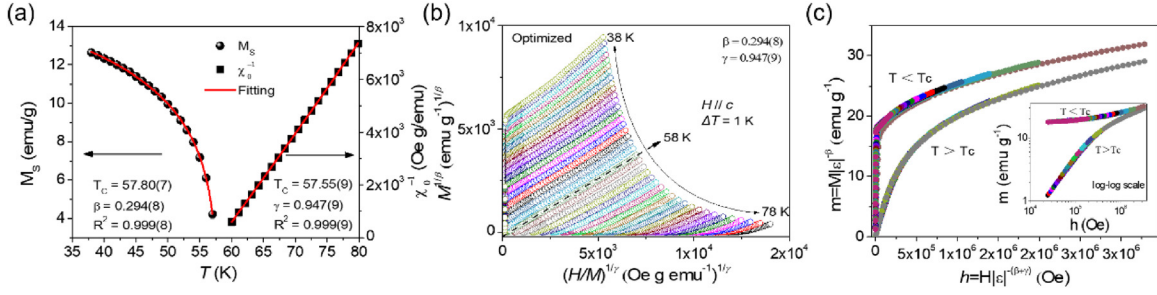
**FIG. 4.** (a) Temperature dependence of the spontaneous magnetization $M_S(T)$ (left) and the inverse initial susceptibility $\chi_0^{-1}(T)$ (right). (b) The modified Arrott plot using $\beta$ and $\gamma$ obtained by the iMAP method. (c) Scaling plots of $m$ vs $h$ below and above $T_C$. The inset is the logarithmic form of the plot.

The scaling equation indicates that through proper selection of critical exponents, all $M(H)$ curves can be collapsed into two independent branches above and below $T_C$. Figure 4(c) presents the scaling results using the critical exponents obtained by the iMAP method, which shows two general branches that conform to Eq. (8). The inset of Fig. 4(c) is the logarithmic form of the scale, which also collapses into two general branches.

In addition, the MEC method provides an alternative approach for determining critical exponents. Unlike the previously discussed methods that directly fit power-law dependencies of magnetic parameters, the MEC method extracts the critical exponents by correlating the field dependence of the magnetic entropy change with critical exponents. The specific steps for determining the critical exponents of the CrVI$_6$ crystal using the MEC method are as follows: Obtaining the change of magnetic entropy ($\Delta S_M$) is the first step to fit the critical exponents using the MEC method. $\Delta S_M$ can be calculated by the following formula using the isothermal magnetization data [Fig. 3(a)]:[54]

$$\Delta S_M(T,H) = \int_0^H (\partial S/\partial H)_T dH = \int_0^H (\partial M/\partial T)_H dH, \quad (9)$$

where $(\partial S/\partial H)_T = (\partial M/\partial T)_H$ is based on Maxwell's relation. Considering the interval of the magnetic field and temperature is sufficiently small, Eq. (9) can be rewritten as[55]

$$\Delta S_M(T,H) = \left( \int_0^H M(T_{i+1},H)dH - \int_0^H M(T_i,H)dH \right) \bigg/ (T_{i+1}-T_i). \quad (10)$$

The obtained temperature-dependent $\Delta S_M$ plots under different magnetic fields are illustrated in Fig. 5(a). When $\Delta S_M$ is obtained, a series of fitted exponents can be extracted from the following equations for a second-order phase transition:[56,57]

$$|\Delta S_M^{\max}| \propto H^n, \quad (11)$$

$$RCP \propto H^c, \quad (12)$$

where $|\Delta S_M^{\max}|$ is the maximum absolute value of $\Delta S_M$, $RCP = |\Delta S_M^{\max}| \times \delta T_{FWHM}$ is the relative cooling power, $\delta T_{FWHM}$ is the full-width at half maximum. The fitted exponents, n and c, can be used to determine the critical exponents using the following equations:[45]

$$n = 1 + \frac{\beta - 1}{\beta + \gamma}, \quad (13)$$

$$c = 1 + \frac{1}{\delta}. \quad (14)$$

Figure 5(b) shows the fitting results of $|\Delta S_M^{\max}|$ and $RCP$, the obtained fitted exponents are n = 0.527(5) and c = 1.203(6). Based on Eqs. (6), (13), and (14), the critical exponents are calculated to be $\beta = 0.30(1)$, $\gamma = 1.17(7)$, and $\delta = 4.91(1)$. In the MEC method, additional effects, for example, the Jahn–Teller effect, can impact the entropy change,[58,59] leading to deviations in critical exponents compared to the iMAP method.

For a second-order phase transition, by scaling equation, the expression of $\Delta S_M$ can be rewritten as[60,61]

$$\Delta S_M(T,H) = H^{(1-\alpha)/\Delta} g(\varepsilon/H^{1/\Delta}), \quad (15)$$
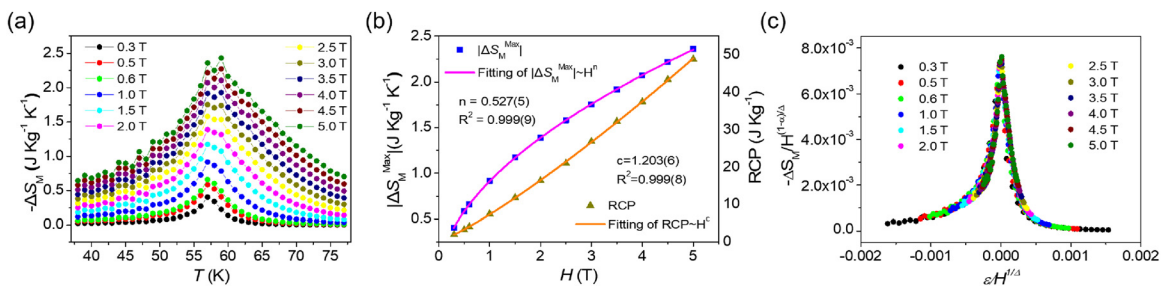


**FIG. 5.** (a) Temperature-dependent $-\Delta S_M$ under different magnetic fields. (b) Magnetic field dependence of parameters from $-\Delta S_M(T,H)$ with the fitted curves of $|\Delta S_M^{\max}|$ and $RCP$. (c) Scaling of the $-\Delta S_M(T,H)$ curves plotted by $-\Delta S_M/H^{(1-\alpha)/\Delta}$ vs $\varepsilon/H^{1/\Delta}$.

$$\alpha = 2 - 2\beta - \gamma, \tag{16}$$

$$\Delta = \delta \times \beta, \tag{17}$$

where $\varepsilon = (T - T_C)/T_C$ is the reduced temperature, and $g$ represents a regular scaling function. With appropriate selections of critical exponents, the plots of $-\Delta S_M/H^{(1-\alpha)/\Delta}$ vs $\varepsilon/H^{1/\Delta}$ should collapse onto a single curve. By substituting the critical exponents obtained by MEC into the above-mentioned equations and plotting the results in Fig. 5(c), the plots under different external magnetic fields (0.3–5 T) collapse into a single curve, which proves the reliability and effectiveness of the critical exponents obtained by the MEC method.

Finally, the critical exponents of $CrVI_6$, $CrI_3$, $VI_3$, and theoretical models are summarized in Table I for convenient comparison. The analysis concentrates on the critical exponents derived from both MEC and iMAP methods, as these have been rigorously validated through scaling equations. For the iMAP method, we find that the critical exponents of $CrVI_6$ lie between those of $CrI_3$ and $VI_3$ obtained by the iMAP method, suggesting intercorrelated interactions from Cr and V in this system. Taroni $et$ $al.$ reported a comprehensive study of the critical exponents of 2D magnets and concluded that the critical exponent $\beta$ should be within the window of $0.1 < \beta < 0.25$.[62] However, the critical exponent $\beta$ of $CrVI_6$ is much greater than 0.25 and approaches the theoretical value predicted for the 3D Ising model. It demonstrates non-negligible interlayer coupling and short-range interactions in $CrVI_6$ crystals, consistent with the conclusions derived from the MAP method. Meanwhile, the result approaching the Ising type is consistent with the strong uniaxial anisotropy found in the $CrVI_6$, as discovered in the experiment. The $\gamma$ value of $CrVI_6$ closely matches $\gamma = 1$ for mean-field or tricritical mean-field with long-range interactions, indicating that long-range interactions dominate in this system. Overall, the $\beta$ value of $CrVI_6$ falls between those of the 3D Ising model and the tricritical mean-field model, while its $\gamma$ value is closer to the tricritical mean-field model. This suggests a crossover behavior between 3D Ising-type and tricritical mean-field-type interactions in $CrVI_6$, which indicates a competition and coexistence of short-range and long-range interactions, reflecting the complex magnetic interactions in the system. For the MEC method, while the $\beta$ value shows results similar to iMAP, the $\gamma$ values lie between the 3D Ising model and the tricritical mean-field model, which suggests that the system may exhibit extended types of exchange interactions beyond the nearest neighbors. Although minor discrepancies exist between the critical exponents

obtained by these two methods, the MEC results independently confirm the crossover behavior between 3D Ising and tricritical mean-field regimes in $CrVI_6$. This agreement robustly demonstrates the coexistence of both short-range and long-range magnetic interactions in $CrVI_6$, revealing the inherently complex nature of its magnetic coupling mechanisms.

To gain further insights into the critical behaviors of $CrVI_6$, the renormalization group theory was adopted.[63,64] For itinerant electrons, the exchange interaction between magnetic spins exhibits a spatial decay with respect to the distance $r$, characterized by the relationship $J(r) \approx r^{-(d+\sigma)}$, where $d$ denotes the spatial dimensionality and $\sigma$ is a positive constant that quantifies the range of the exchange interaction. Leveraging this renormalization group theory, the critical exponent $\gamma$ can be forecasted by the following correlation:

$$\gamma = 1 + \frac{4(n+2)}{d(n+8)}\Delta\sigma$$

$$+ \frac{8(n+2)(n-4)}{d^2(n+8)^2}\left[1 + \frac{2G\left(\frac{d}{2}\right)(7n+20)}{(n-4)(n+8)}\right]\Delta\sigma^2, \tag{18}$$

where $\Delta\sigma = \left(\sigma - \frac{d}{2}\right)$, $G\left(\frac{d}{2}\right) = 3 - \left(\frac{1}{4}\right)\left(\frac{d}{2}\right)^2$, and $n$ is the spin dimensionality. For a 3D system ($d = 3$), $J(r) \approx r^{-(3+\sigma)}$. When $\sigma \leq \frac{3}{2}$, this situation corresponds to the long-range mean-field model, leading to a scaling relationship of $J(r) \propto r^{-4.5}$. On the contrary, when $\sigma \geq 2$, it corresponds to the short-range 3D Heisenberg model, resulting in $J(r) \propto r^{-5}$. According to the specific value of $\{d: n\}$, the $\sigma$ parameter can be evaluated by Eq. (18). The obtained $\sigma$ enables the derivation of the other remaining critical exponents of the system through the utilization of the following relationships: $\nu = \gamma/\sigma$, $\alpha = 2 - \nu d$, $\beta = (2 - \alpha - \gamma)/2$, and $\delta = 1 + (\gamma/\beta)$. The degree of agreement between these derived critical exponents and the original critical exponents serves as an indicator of which $\{d: n\}$ and $\sigma$ best represent the system. It has been determined that, for $CrVI_6$, $\sigma = 1.80$ is obtained when $\{d: n\} = \{3:1\}$ produces the critical exponents by the MEC method and $\sigma = 1.40$ is obtained when $\{d: n\} = \{3:3\}$ produces the critical exponents by the iMAP method. For the MEC method, the calculated $J(r) \approx r^{-4.80}$ lies between the long-range and short-range model, consistent with the situation where $\gamma$ obtained by the MEC method lies between the 3D-ising model and the mean-field model.

**TABLE I.** Comparison of critical exponents of $CrVI_6$, $CrI_3$, and $VI_3$ obtained from various theoretical models. The iMAP, KFP, CI, and MEC denote the iterative modified Arrott plot, Kouvel–Fisher plot, critical isotherm, and magnetic entropy change, respectively.

| System/model | Technique | $T_C$ (K) | $\beta$ | $\gamma$ | $\delta$ |
|---|---|---|---|---|---|
| $CrVI_6$ (this work) | CI | $\cdots$ | $\cdots$ | $\cdots$ | 3.923(8) |
| $CrVI_6$ (this work) | KFP | 59.7 | 0.295(7) | 0.904(6) | 4.05(9) |
| $CrVI_6$ (this work) | iMAP | 57.8 | 0.294(8) | 0.947(9) | 4.21(5) |
| $CrVI_6$ (this work) | MEC | 58.2 | 0.30(1) | 1.17(7) | 4.91(1) |
| $CrI_3$[65] | iMAP | 64.0 | 0.325 | 0.825 | 3.538 |
| $VI_3$[66] | iMAP | 50.1 | 0.244(5) | 1.028(1) | 5.24(2) |
| 3D XY | Theory | $\cdots$ | 0.345 | 1.316 | 4.81 |
| 3D Ising | Theory | $\cdots$ | 0.325 | 1.240 | 4.82 |
| Tricritical mean-field | Theory | $\cdots$ | 0.25 | 1 | 5 |

For the iMAP method, the calculated $J(r) \approx r^{-4.40}$ demonstrates a predominantly long-range interaction-dominated scenario, consistent with the situation where $\gamma$ obtained by the iMAP method is approximate to the mean-field model. These findings provide further evidence for complex magnetic interactions with the coexistence of short-range and long-range interactions in $CrVI_6$, as revealed by critical exponents analysis.

Additionally, the coexistence of the long-range RKKY (Ruderman–Kittel–Kasuya–Yosida) interaction and the short-range exchange interaction in the $PrMn_2Ge_2$ system has been reported to be a possible origin of its topological spin structure.[28] The Dzyaloshinskii–Moriya interaction (DMI) experimentally found in $CrVI_6$[25] and the spin–orbit coupling theoretically predicted in $CrVI_6$[23] are both likely to increase the complexity of the magnetic interactions, corroborated by the critical behaviors reported in this work. Inspired by the case of $PrMn_2Ge_2$, the coexistence of short-range and long-range interactions with interlayer couplings can serve as one of the reasons driving the topological effects in $CrVI_6$.

In this work, we have grown ferromagnetic $CrVI_6$ single crystals with strong perpendicular magnetocrystalline anisotropy, the $T_C$ of which is determined to be 58.2 K. The critical exponents are observed as $\beta = 0.294(8)$, $\gamma = 0.947(9)$, and $\delta = 4.21(5)$ for $CrVI_6$ crystals, which indicate that the magnetism of $CrVI_6$ follows the crossover behavior between the 3D Ising and the tricritical mean-field type interactions. After the scaling process, the isothermal magnetization curves below and above the critical temperatures collapse into two independent universal branches, which signifies the reliability of the estimation of critical exponents. This study of the magnetic phase transition and critical behavior of $CrVI_6$ provides valuable insights into the magnetic properties of the 2D magnetic system with element mutation of Cr- and V-based trihalides and enhances the comprehension of its nontrivial topology.

See the supplementary material for the experimental details, the acquisition of spontaneous magnetization and inverse initial susceptibility, and modified Arrott plots for $CrVI_6$.

## AUTHOR DECLARATIONS
### Conflict of Interest

The authors have no conflict to disclose.

### Author Contributions

Qiaoqiao Wang and Hanzhang Zhao contributed equally to this work.

**Qiaoqiao Wang:** Conceptualization (equal); Data curation (equal); Formal analysis (equal); Investigation (equal); Methodology (equal); Project administration (equal); Software (equal); Validation (equal); Visualization (equal); Writing – original draft (equal); Writing – review & editing (equal). **Hanzhang Zhao:** Conceptualization (equal); Data curation (equal); Formal analysis (equal); Investigation (equal); Methodology (equal); Project administration (equal). **Xuegang Chen:** Project administration (equal); Supervision (equal); Validation (equal); Writing – review & editing (equal). **Feiyan Hou:** Project administration (equal); Supervision (equal); Validation (equal); Visualization (equal); Writing – review & editing (equal). **Tao Li:** Conceptualization (equal); Formal analysis (equal); Funding acquisition (equal); Investigation (equal); Methodology (equal); Project administration (equal); Resources (equal); Software (equal); Supervision (equal); Validation (equal); Visualization (equal); Writing – original draft (equal); Writing – review & editing (equal). **Tai Min:** Funding acquisition (equal); Project administration (equal); Writing – original draft (equal); Writing – review & editing (equal).

## DATA AVAILABILITY

The data that support the findings of this study are available from the corresponding authors upon reasonable request.

## REFERENCES

[1] B. Huang, G. Clark, E. Navarro-Moratalla, D. R. Klein, R. Cheng, K. L. Seyler, D. Zhong, E. Schmidgall, M. A. McGuire, D. H. Cobden, W. Yao, D. Xiao, P. Jarillo-Herrero, and X. Xu, Nature **546**, 270 (2017).

[2] C. Gong, L. Li, Z. Li, H. Ji, A. Stern, Y. Xia, T. Cao, W. Bao, C. Wang, Y. Wang, Z. Q. Qiu, R. J. Cava, S. G. Louie, J. Xia, and X. Zhang, Nature **546**, 265 (2017).

[3] Y. Deng, Y. Yu, Y. Song, J. Zhang, N. Z. Wang, Z. Sun, Z. Yi, Y. Z. Wu, S. Wu, J. Zhu, J. Wang, X. H. Chen, and Y. Zhang, Nature **563**, 94 (2018).

[4] D. Ghazaryan, M. T. Greenaway, Z. Wang, V. H. Guarochico-Moreira, I. J. Vera-Marun, J. Yin, Y. Liao, S. V. Morozov, O. Kristanovski, A. I. Lichtenstein, M. I. Katsnelson, F. Withers, A. Mishchenko, L. Eaves, A. K. Geim, K. S. Novoselov, and A. Misra, Nat. Electron. **1**, 344 (2018).

[5] T. Kong, K. Stolze, E. I. Timmons, J. Tao, D. Ni, S. Guo, Z. Yang, R. Prozorov, and R. J. Cava, Adv. Mater. **31**, 1808074 (2019).

[6] S. Tian, J.-F. Zhang, C. Li, T. Ying, S. Li, X. Zhang, K. Liu, and H. Lei, J. Am. Chem. Soc. **141**, 5326 (2019).

[7] Y. Deng, Y. Yu, M. Z. Shi, Z. Guo, Z. Xu, J. Wang, X. H. Chen, and Y. Zhang, Science **367**, 895 (2020).

[8] L. Meng, Z. Zhou, M. Xu, S. Yang, K. Si, L. Liu, X. Wang, H. Jiang, B. Li, P. Qin, P. Zhang, J. Wang, Z. Liu, P. Tang, Y. Ye, W. Zhou, L. Bao, H.-J. Gao, and Y. Gong, Nat. Commun. **12**, 809 (2021).

[9] G. Zhang, F. Guo, H. Wu, X. Wen, L. Yang, W. Jin, W. Zhang, and H. Chang, Nat. Commun. **13**, 5067 (2022).

[10] H. Wu, L. Yang, G. Zhang, W. Jin, B. Xiao, W. Zhang, and H. Chang, Small Methods **8**, 2301524 (2024).

[11] M. Alghamdi, M. Lohmann, J. Li, P. R. Jothi, Q. Shao, M. Aldosary, T. Su, B. P. T. Fokwa, and J. Shi, Nano Lett. **19**, 4400 (2019).

[12] W. Jin, G. Zhang, H. Wu, L. Yang, W. Zhang, and H. Chang, ACS Appl. Mater. Interfaces **15**, 36519 (2023).

[13] S. N. Kajale, T. Nguyen, C. A. Chao, D. C. Bono, A. Boonkird, M. Li, and D. Sarkar, Nat. Commun. **15**, 1485 (2024).

[14] H. Pan, A. K. Singh, C. Zhang, X. Hu, J. Shi, L. An, N. Wang, R. Duan, Z. Liu, S. P. Parkin, P. Deb, and W. Gao, InfoMat **6**, e12504 (2024).

[15] I. Shin, W. J. Cho, E. S. An, S. Park, H. W. Jeong, S. Jang, W. J. Baek, S. Y. Park, D. H. Yang, J. H. Seo, G. Y. Kim, M. N. Ali, S. Y. Choi, H. W. Lee, J. S. Kim, S. D. Kim, and G. H. Lee, Adv. Mater. **34**, 2101730 (2022).

[16] L. Zhang, X. Huang, H. Dai, M. Wang, H. Cheng, L. Tong, Z. Li, X. Han, X. Wang, L. Ye, and J. Han, Adv. Mater. **32**, 2002032 (2020).

[17] B. Zhao, R. Ngaloy, S. Ghosh, S. Ershadrad, R. Gupta, K. Ali, A. M. Hoque, B. Karpiak, D. Khokhriakov, C. Polley, B. Thiagarajan, A. Kalaboukhov, P. Svedlindh, B. Sanyal, and S. P. Dash, Adv. Mater. **35**, 2209113 (2023).

[18] W. Zhu, H. Lin, F. Yan, C. Hu, Z. Wang, L. Zhao, Y. Deng, Z. R. Kudrynskyi, T. Zhou, Z. D. Kovalyuk, Y. Zheng, A. Patanè, I. Žutić, S. Li, H. Zheng, and K. Wang, Adv. Mater. **33**, 2104658 (2021).

[19] M. A. McGuire, H. Dixit, V. R. Cooper, and B. C. Sales, Chem. Mater. **27**, 612 (2015).

[20] K. L. Seyler, D. Zhong, D. R. Klein, S. Gao, X. Zhang, B. Huang, E. Navarro-Moratalla, L. Yang, D. H. Cobden, M. A. McGuire, W. Yao, D. Xiao, P. Jarillo-Herrero, and X. Xu, Nat. Phys. **14**, 277 (2017).

[21]Y. Xu, A. Ray, Y.-T. Shao, S. Jiang, K. Lee, D. Weber, J. E. Goldberger, K. Watanabe, T. Taniguchi, D. A. Muller, K. F. Mak, and J. Shan, Nat. Nanotechnol. **17**, 143 (2022).

[22]D. Soler-Delgado, F. Yao, D. Dumcenco, E. Giannini, J. Li, C. A. Occhialini, R. Comin, N. Ubrig, and A. F. Morpurgo, Nano Lett. **22**, 6149 (2022).

[23]H. Zhang, P. Cui, X. Xu, and Z. Zhang, arXiv:2112.10924 (2021).

[24]S. Pan, Y. Bai, J. Tang, P. Wang, Y. You, G. Xu, and F. Xu, J. Alloys Compd. **908**, 164573 (2022).

[25]X. Li, C. Liu, Y. Zhang, S. Zhang, H. Zhang, Y. Zhang, W. Meng, D. Hou, T. Li, C. Kang, F. Huang, R. Cao, D. Hou, P. Cui, W. Zhang, T. Min, Q. Lu, X. Xu, Z. Sheng, B. Xiang, and Z. Zhang, Nat. Phys. **20**, 1145 (2024).

[26]X. Yang, J. Zhao, F. Meng, A. Rahman, Y. Qin, J. Fan, L. Pi, Z. Tian, H. Du, L. Zhang, and Y. Zhang, Phys. Rev. B **103**, 214401 (2021).

[27]H. C. Chauhan, B. Kumar, A. Tiwari, J. K. Tiwari, and S. Ghosh, Phys. Rev. Lett. **128**, 015703 (2022).

[28]M. Song, J. Zhao, C. Liu, M. He, Y. Wang, Y. Han, L. Ling, L. Cao, L. Zhang, Z. Qu, and Y. Xiong, Appl. Phys. Lett. **120**, 092402 (2022).

[29]F. Meng, W. Liu, A. Rahman, J. Zhang, J. Fan, C. Ma, M. Ge, T. Yao, L. Pi, L. Zhang, and Y. Zhang, Phys. Rev. B **107**, 144425 (2023).

[30]G. Garton, M. J. M. Leask, W. P. Wolf, and A. F. G. Wyatt, J. Appl. Phys. **34**, 1083 (1963).

[31]Y. Liu and C. Petrovic, Phys. Rev. B **97**, 174418 (2018).

[32]S. Son, M. J. Coak, N. Lee, J. Kim, T. Y. Kim, H. Hamidov, H. Cho, C. Liu, D. M. Jarvis, P. A. C. Brown, J. H. Kim, C.-H. Park, D. I. Khomskii, S. S. Saxena, and J.-G. Park, Phys. Rev. B **99**, 041402 (2019).

[33]K. Spurgeon, G. Kozlowski, M. A. Susner, Z. Turgut, and J. Boeckl, SCIREA J. Electr. Eng. **5**, 141 (2020).

[34]J. Valenta, M. Kratochvílová, M. Míšek, K. Carva, J. Kaštil, P. Doležal, P. Opletal, P. Čermák, P. Proschek, K. Uhlířová, J. Prchal, M. J. Coak, S. Son, J. G. Park, and V. Sechovský, Phys. Rev. B **103**, 054424 (2021).

[35]X. X. Zhang, G. H. Wen, F. W. Wang, W. H. Wang, C. H. Yu, and G. H. Wu, Appl. Phys. Lett. **77**, 3072 (2000).

[36]H. E. Stanley, Rev. Mod. Phys. **71**, S358 (1999).

[37]S. N. Kaul, J. Magn. Magn. Mater. **53**, 5–53 (1985).

[38]M. E. Fisher, Rep. Prog. Phys. **30**, 615 (1967).

[39]S. Mondal, N. Khan, S. M. Mishra, B. Satpati, and P. Mandal, Phys. Rev. B **104**, 094405 (2021).

[40]X. Yang, J. Pan, W. Gai, Y. Tao, H. Jia, L. Cao, and Y. Cao, Phys. Rev. B **105**, 024419 (2022).

[41]F. K. Lotgering and E. W. Gorter, J. Phys. Chem. Solids **3**, 238 (1957).

[42]J. S. Kouvel and M. E. Fisher, Phys. Rev. **136**, A1626 (1964).

[43]A. Arrott and J. E. Noakes, Phys. Rev. Lett. **19**, 786 (1967).

[44]A. K. Pramanik and A. Banerjee, Phys. Rev. B **79**, 214426 (2009).

[45]V. Franco and A. Conde, Int. J. Refrig. **33**, 465 (2010).

[46]L. P. Kadanoff, Phys. Phys. Fiz. **2**, 263 (1966).

[47]A. Arrott, Phys. Rev. **108**, 1394 (1957).

[48]J. Le Guillou and J. Zinn-Justin, Phys. Rev. B **21**, 3976 (1980).

[49]Y. Liu and C. Petrovic, Phys. Rev. B **97**, 014420 (2018).

[50]H. Liu, J. Fan, F. Qian, Y. Ji, A. Rahman, R. Tang, L. Zhang, L. Ling, Y. Zhu, and H. Yang, Phys. Chem. Chem. Phys. **23**, 4912 (2021).

[51]X. Yang, J. Pan, S. Liu, M. Yang, L. Cao, D. Chu, and K. Sun, Phys. Rev. B **103**, 104405 (2021).

[52]A. Rahman, M. U. Rehman, M. Kiani, H. Zhao, J. Wang, Y. Lu, K. Ruan, R. Dai, Z. Wang, L. Zhang, J. Wang, and Z. Zhang, Phys. Rev. B **105**, 144413 (2022).

[53]X. Yang, J. Pan, X. He, and D. Chu, Phys. Rev. B **109**, 094408 (2024).

[54]V. K. Pecharsky and K. A. Gschneidner Jr., J. Magn. Magn. Mater **200**, 44 (1999).

[55]M. H. Phan and S. C. Yu, J. Magn. Magn. Mater. **308**, 325 (2007).

[56]V. Franco, J. S. Blázquez, and A. Conde, Appl. Phys. Lett. **89**, 222512 (2006).

[57]V. Franco, A. Conde, J. Romero-Enrique, and J. Blázquez, J. Phys.: Condens. Matter **20**, 285207 (2008).

[58]J. Mira, J. Rivas, L. E. Hueso, F. Rivadulla, and M. A. López Quintela, J. Appl. Phys. **91**, 8903 (2002).

[59]J. Yang, Y. P. Lee, and Y. Li, J. Appl. Phys. **102**, 033913 (2007).

[60]H. E. Stanley, *Phase Transitions and Critical Phenomena* (Clarendon Press, Oxford, 1971), Vol. 7.

[61]Y. Su, Y. Sui, J. G. Cheng, J. S. Zhou, X. Wang, Y. Wang, and J. B. Goodenough, Phys. Rev. B **87**, 195102 (2013).

[62]A. Taroni, S. T. Bramwell, and P. C. Holdsworth, J. Phys.: Condens. Matter **20**, 275233 (2008).

[63]S. F. Fischer, S. N. Kaul, and H. Kronmüller, Phys. Rev. B **65**, 064443 (2002).

[64]M. E. Fisher, S.-k. Ma, and B. G. Nickel, Phys. Rev. Lett. **29**, 917 (1972).

[65]G. T. Lin, X. Luo, F. C. Chen, J. Yan, J. J. Gao, Y. Sun, W. Tong, P. Tong, W. J. Lu, Z. G. Sheng, W. H. Song, X. B. Zhu, and Y. P. Sun, Appl. Phys. Lett. **112**, 072405 (2018).

[66]Y. Liu, M. Abeykoon, and C. Petrovic, Phys. Rev. Res. **2**, 013013 (2020).

22 September 2025 06:46:04